11th International Symposium on Turbulence and Shear Flow Phenomena (TSFP11)
Southampton, UK, July 30 to August 2, 2019

CHARACTERIZING TURBULENCE IN MULTI-ROTOR WIND TURBINE WAKES USING LARGE EDDY SIMULATION

Niranjan S. Ghaisas
Center for Turbulence Research
Stanford University
nghaisas@stanford.edu

Aditya S. Ghate
Department of Aeronautics and Astronautics
Stanford University
aditya90@stanford.edu

Sanjiva K. Lele
Department of Aeronautics and Astronautics,
Department of Mechanical Engineering,
and Center for Turbulence Research
Stanford University
lele@stanford.edu

INTRODUCTION

Wind energy has seen a rapid growth in recent years. Understanding the turbulent wakes of wind turbines is key to ensuring further growth of wind energy. This is because the smaller wind speed in the wakes reduces the amount of energy available for downstream turbines, while the increased turbulence leads to reduced turbine lifetime by increasing fatigue loads on the downstream turbines. Multi-rotor wind turbine configurations, where more than one rotor is mounted on a single tower, have received attention recently primarily due to the potential for structural advantages (Jaimeson & Branney, 2012, 2014). The advantages afforded by a 4-rotor turbine with respect to the rate of wake recovery were described in our previous study (Ghaisas *et al.*, 2018). In this work, the motivation is to study effects of spacing between the tips of the rotors on the flow field. The analysis will focus on the turbulence in the wakes and their merging process.

Numerical Methodology

The simulation tool used solves the standard LES-filtered incompressible Navier-Stokes equations on a structured uniform Cartesian mesh using Fourier-collocation in x and y directions, sixth-order staggered compact finite-differences in the z direction and a total variation diminishing (TVD) fourth-order Runge-Kutta time-stepping scheme. The effect of sub-filter scales is modeled using the anisotropic minimum dissipation (AMD) model (Rozema *et al.*, 2015). Viscous effects are smaller than inertial effects by approximately 10 orders of magnitude and are neglected throughout this paper. Turbine forces are modeled using an actuator drag-disk approach. The force exerted in the x direction is given by $F_1 = -0.5 A_{rot} C_T' u_1^2$, where u_1 is the instantaneous LES-filtered velocity and C_T' is the local thrust coefficient. Non-periodic boundary conditions in the x direction can be simulated using a fringe/buffer region forcing technique (Nordström *et al.*, 1999). Different aspects of the code have been validated over several previously published studies (Ghate & Lele, 2017; Ghaisas *et al.*, 2017, 2018).

Two sets of simulations are carried out in this paper. In the first set, 1-rotor and 4-rotor turbines are placed in a turbulent half-channel to mimic wind turbines subjected to atmospheric boundary layer (ABL) turbulence. Numerical details, boundary conditions, and the concurrent precursor-simulation method, along with the domain size and placement of turbines for this set of simulations are exactly as described in Ghaisas *et al.* (2018). Briefly, half-channel simulations with a boundary layer height $H = 1000$ m, friction velocity $u_* = 0.45$ m/s and surface roughness height $z_0 = 0.1$ m are used to drive the wind turbine simulations. The turbine disks are located in the lower one-tenth portion of the ABL in the vertical direction, and are virtually unimpeded in the spanwise direction. The setup allows for studying up to 20 1-rotor diameters downstream of the turbine disks before numerical artifacts associated with the fringe region forcing contaminate the results. Following the grid convergence study reported in Ghaisas *et al.* (2018), all simulations are carried out using $256 \times 128 \times 160$ grid points per domain. The spinup and averaging times are also as reported in Ghaisas *et al.* (2018). All results reported are non-dimensionalized with H and u_* as length and velocity scales, respectively.

In the second set of simulations, turbine actuator disks (AD) are subjected to a flow field with a steady mean advection $(U, 0, 0)$, superimposed with fluctuations from a homogeneous isotropic turbulence (HIT) concurrent simulation. The HIT is forced such that the turbulence intensity (TI) of the flow incident on the turbine ADs is approximately 4% of the mean. The domain, boundary conditions, and other numerical details are identical to our previous study Ghate *et al.* (2018). Periodic conditions are maintained in both the cross-stream directions (y, z), while two fringe regions are used in the axial (x) direction to mimic the effect of non-periodicity. The first fringe region forces the flow to laminarize, while the second applies the HIT field to the laminarized flow, effectively ensuring that the inflow to the full domain attains the desired turbulent state. The effective domain size in the x direction allows for studying the wakes for approximately 9 1-rotor diameters downstream of the turbine disks. The concurrent HIT uses 128^3 grid points while the main simulation utilizes 640×128^2 grid points. All results for this set of studies are non-dimensionalized with the turbine diameter D and the mean inflow velocity U as length and velocity scales, respectively.

Different geometric features of the turbine models used are shown in Figure 1. All simulations use $H_T = D = 2d = 0.1H$, and a fixed thrust coefficient, $C_T' = 1.33$, for all rotors. A 1-rotor (diameter D) simulation is carried out as a baseline, against which the 4-rotor (diameters $d = D/2$) simulations are compared. In the first set of simulations, seven 4-rotor turbines are considered, with different spacings between the tips of rotors, $s_h/d = s_v/d = s/d = (0, 0.05, 0.1, 0.2, 0.25, 0.5, 1.0)$. In the second set, a 1-rotor simulation is compared to 4-rotor turbines with tip spacings $s_h/d = s_v/d = s/d = (0.1, 0.25, 0.5)$.

Results

Turbine Actuator Disks in Atmospheric Boundary Layer

Figure 3 shows contours of the mean velocity deficit and the turbulent kinetic energy (TKE) at the plane along the turbine centerline in the spanwise (y) direction. The velocity deficit at each point is calculated as $\Delta U(x,y,z) = U(-1D,y,z) - U(x,y,z)$. The deficits are large close to the turbine disks, and gradually decrease in intensity as low-momentum fluid is entrained into the wake. Comparing Figures 3(a) and (c), it is apparent that the combined wake of the 4-rotor turbine dissipates faster than the wake of the 1-rotor turbine.

Axial variation of disk-averaged mean velocity deficits is shown in Figure 2. These profiles are computed by averaging the pointwise deficits over the rotor area (in the $y-z$ plane) at each axial (x) location. The averages are computed over one circle for the 1-rotor case, and over four non-contiguous circles for the 4-rotor cases. The total area of integration, and the total frontal area of the rotors, is equal to $\pi D^2/4$ in all cases.

Figure 2 shows that the velocity deficits are smaller for all 4-rotor cases compared to the 1-rotor case, consistent with the contour plots in Figures 3(a) and (c). This implies that the rate of wake recovery is faster for the 4-rotor turbines as compared to the 1-rotor turbine. The rate of recovery increases with increasing tip spacing, s. These results are consistent with, and expand on, those reported in Ghaisas *et al.* (2018), where fewer tip spacings were considered. The velocity deficits corresponding to the 1-rotor and $s/d = 1$ cases envelope the velocity deficits corresponding to intermediate tip spacings.

Disk-averaged added TKE profiles are shown in Figure 4. Added TKE is defined as $\Delta TKE(x,y,z) = TKE(x,y,z) - TKE(-1D,y,z)$, which is disk-averaged similar to the disk-averaged velocity deficit. In general, the added TKE is smaller for the 4-rotor cases than for the 1-rotor case. Unlike for the deficits, the 1-rotor and $s/d = 1$ results no longer envelope the added TKE results for the intermediate tip spacings. Figure 4 reflects the complex process of merging of the individual wakes, which is strongly dependent on the tip spacing.

The contour plots in Figure 6 show this dependence of merging of wakes on the tip spacing. In the very near-wake region ($x/D = 2$), the added TKE values are positive primarily near the tops of the turbine rotors. Significant interaction is seen between the wakes of the four rotors in the $s/d = 0.1$ case at this axial location. On the other hand, in the $s/d = 0.5$ case, the wakes are almost independent at $x/D = 2$, but start interacting at $x/D = 4$.

The complex spatial distribution of the TKE shown in Figures 3 and 6 and the disk-averaged added TKE profiles in Figure 4 have implications for design of multi-rotor wind farms. Figure 5 shows the added TKE level that a hypothetical 4-rotor turbine placed downstream of a 4-rotor turbine would be subjected to, as a function of the tip spacing. This figure shows, for example, that a tip spacing of $s/d = 0.5$ is optimal with respect to the added TKE, if the inter-turbine spacing were to be $6D, 7D$ or $8D$, but is not optimal if the turbines were to be spaced closer than $6D$.

Turbine Actuator Disks Interacting with Homogeneous Isotropic Turbulence

The results of the previous section underscore the importance of understanding the wake recovery and merging processes in the 1-rotor and 4-rotor wind turbine wakes. Highly-resolved simulations of an idealized problem are considered here to facilitate this. A 1-rotor turbine case and three 4-rotor turbine cases are studied. In each case, the turbines are subjected to a mean advective flow field, superimposed with homogeneous isotropic turbulent fluctuations. Contour plots of the $13-$ component of the anisotropy tensor, $b_{ij} = R_{ij}/R_{kk} - \delta_{ij}/3$, are shown in Figure 7. Here, $R_{ij} = \overline{u_i' u_j'}$, denotes the Reynolds stress tensor. Shear layers that originate at the turbine disks and grow in thickness with increasing spatial distance from the disk are clearly seen.

For each turbine rotor disk, we first construct a streamtube that exactly encloses the disk. This defines one contiguous streamtube for the 1-rotor turbine, and 4 non-contiguous streamtubes for the 4-rotor turbines. The axial variation of the total area enclosed by the streamtubes is shown in Figure 8. In each case, the total area of the streamtubes equals $\pi D^2/4$ at the turbine location. With increasing spatial distance from the turbine disks, the streamtube areas first increase as the streamlines diverge, and then decrease as the streamlines converge. The peak of the streamtube area is reached earlier for the 4-rotor turbines. Consequently, beyond $x/D = 1$, the streamtube areas are smaller for the 4-rotor turbines, as compared to for the 1-rotor turbine. The streamtube areas are also dependent on the tip spacing, with smaller areas for larger tip spacings.

The terms in the mean kinetic energy (MKE) equation,

$$0 = -\bar{u}_j \partial_j (\bar{u}_i \bar{u}_i)/2 + \partial_j \left[-\bar{p}\bar{u}_j - \bar{u}_i \bar{\tau}_{ij} - \bar{u}_i \overline{u_i' u_j'} \right] + \overline{u_i' u_j'} \partial_j \bar{u}_i + \bar{\tau}_{ij} \partial_j \bar{u}_i + \bar{u}_i \bar{F}_i, \quad (1)$$

are mean advection, pressure transport, SGS transport, Reynolds Stress transport, TKE production, SGS dissipation and turbine actuator disk work, progressively from left to right. Here, u_i and p denote the LES-filtered velocity field and the LES-filtered pressure fields, respectively. The overbar denotes the time-averaging operator, and prime denotes fluctuation of an LES-filtered quantity around its time average. Different terms in this equation are averaged over time and the streamtube areas, and are presented as profiles along the axial direction in Figure 9. The region very close to the turbine $x/D < 0.25$ is excluded from the analysis here, since the aim is to focus on the wake.

Figure 9(a) (for 1-rotor turbine) shows that the primary balance is between mean advection, Reynolds Stress transport and pressure transport, while TKE prodcution is small but significant. All other terms can be seen to be very small. In particular, the residual is less than 0.2% of the dominant term at each point, which indicates that the statistics are well-converged. The MKE budgets are qualitatively similar for the 4-rotor cases studied here. The three dominant terms are quantified in Figure 9(b). The mean advection and Reynolds Stress transport terms are strongly sensitive to the tip spacing. Comparing Figure 8 and Figure 9, the location of the peak of the streamtube area correlates strongly with the location where the mean advection changes from positive to negative.

Similar to the MKE equation, the terms in the TKE equation,

$$0 = -\bar{u}_j \partial_j \left(\overline{u_i' u_i'} \right) / 2 + \partial_j \left[-\overline{p' u_j'} - \overline{u_i' \tau_{ij}'} - \left(\overline{u_i' u_i' u_j'} \right) / 2 \right] - \overline{u_i' u_j'} \partial_j \bar{u}_i + \overline{\tau_{ij}' \partial_j u_i'} + \overline{u_i' F_i'}, \quad (2)$$

are mean advection, pressure transport, SGS transport, turbulent transport, TKE production, SGS dissipation and turbine actuator disk work, progressively from left to right. Time- and streamtube-averaged axial profiles of these terms are plotted in Figure 10. Results for the 1-rotor case in Figure 10(a) show that the primary balance of the TKE budget is between TKE production, SGS dissipation and turbulent transport. The pointwise residuals are, once again, smaller than 0.2% of the dominant term, and are indicative of the stationarity of the results.

Figure 10(b) compares the dominant terms in the TKE budget for the 1-rotor turbine and the 4-rotor turbines. TKE production and SGS dissipation are qualitatively similar across the 1-rotor and 4-rotor cases. The turbulent transport is always negative for the 1-rotor case, while it changes from negative to positive at around $x/D \sim 3$ for the 4-rotor cases. This term might appear to be qualitatively dissimilar between the 1-rotor and 4-rotor cases at first sight. However, the turbulent transport term in the 1-rotor budget turns positive further downstream, beyond the scale of this figure, at approximately twice the axial distance where it turns positive for the 4-rotor curves. Similarly, the peak of the SGS dissipation lies at approximately $x/D = 6$ for the 1-rotor case, while those of the 4-rotor cases lie at approximately $x/D = 3$. This indicates that the diameter of the individual rotors (D for 1-rotor case and $d = D/2$ for the 4-rotor cases) is an important length scale controlling the axial evolution of the wakes.

Further insight can be gleaned from the MKE and TKE budget analyses for the 4-rotor turbines. The mean advection and Reynolds Stress transport in Figure 9 and the TKE production and turbulent transport in Figure 10 are independent of the tip spacing close to the turbine ADs, for $x/D < 0.8$, but are sensitive beyond this axial location. The SGS dissipation is relatively insensitive to the tip spacing. This indicates that the larger scales of turbulence, that control mean advection, Reynolds Stress transport, TKE production and turbulent production, are sensitive to the tip spacing. Conversely, the smaller scales that control SGS dissipation, are not sensitive to the tip spacing. The pressure transport term is controlled by the largest imposed geometric scale, which is the rotor diameter, and hence, is not sensitive to the tip spacing.

Conclusions and Outlook

The wakes of multi-rotor wind turbines are studied using large eddy simulation. The focus of this work is on the turbulence generated due to the merging of rotor wakes, and its dependence on the spacing between the tips of the rotors. To this end, 1-rotor and equivalent 4-rotor turbines subjected to ABL turbulence as well as to an idealized inflow involving a HIT turbulence field are studied.

In the ABL-turbine interaction simulations, the velocity deficits in the wakes are found to be sensitive to the tip spacing. The spatial heterogeneity of the TKE distribution in the turbine wakes also varies significantly with varying tip spacing. A consequence of these observations is that the optimal (with respect to wake deficit recovery and fatigue loads) axial spacing between rows of multi-rotor wind turbines is seen to be dependent on the tip spacing. This further implies that design of multi-rotor wind farms should take into account the tip spacing between rotors of the multi-rotor turbines.

The HIT-turbine interaction simulations allow for a detailed study of the energetics of the flow in the wakes of the turbines. Different terms in the MKE and TKE equations are sensitive to different extents to the tip spacing. Further analysis will focus on the distribution of radial fluxes of MKE and TKE along the streamtube. The relative importance of frontal flux over planform flux of kinetic energy is still an open question and an important consideration for design of optimal wind farm layout. Other design considerations, such as co/counter-rotation and yaw misalignment of individual rotors, will be studied in the future using the framework developed here.

REFERENCES

Ghaisas, N., Ghate, A. & Lele, S. K. 2017 Farm efficiency of wind farms: Evaluation using large-eddy simulation. In *10th International Symposium on Turbulence and Shear Flow Phenomena*.

Ghaisas, N., Ghate, A. & Lele, S. K. 2018 Large-eddy simulation of multi-rotor wind turbines. *Journal of Physics: Conference Series* **1037**, 072021.

Ghate, A.S., Ghaisas, N. S., Towne, A. S. & Lele, S. K. 2018 Interaction of small-scale Homogeneous Isotropic Turbulence with an Actuator Disk, AIAA-2018-0753. In *36th Wind Energy Symposium, AIAA Scitech Forum.*

Ghate, A. & Lele, S. 2017 Subfilter-scale enrichment of planetary boundary layer large eddy simulation using discrete Fourier-Gabor modes. *Journal of Fluid Mechanics* **819**, 494–539.

Jaimeson, P. & Branney, M. 2012 Multi-Rotors; A Solution to 20MW and Beyond? *Energy Procedia* **24**, 52–59.

Jaimeson, P. & Branney, M. 2014 Structural Considerations of a 20MW Multi-Rotor Wind Energy System. *Journal of Physics: Conference Series* **555**, 012013.

Nordström, Jan, Nordin, Niklas & Henningson, Dan 1999 The fringe region technique and the fourier method used in the direct numerical simulation of spatially evolving viscous flows. *SIAM Journal on Scientific Computing* **20** (4), 1365–1393.

Rozema, W., Bae, H., Moin, P. & Verstappen, R. 2015 Minimum dissipation models for large eddy simulation. *Physics of Fluids* **27**, 085107.

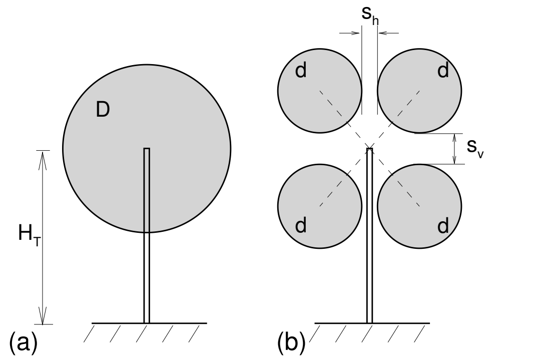

Figure 1. Schematic of (a) conventional 1-rotor and (b) novel 4-rotor turbines. Tower height H_T is identical in both. Diameters are related by $D = 2d$. Spacings between tips are s_h in horizontal and s_v in vertical.

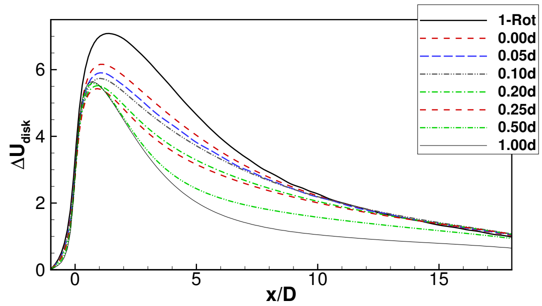

Figure 2. ABL-turbine interaction simulation results. Disk-averaged mean streamwise velocity deficits as a function of axial distance for 1-rotor turbine and 4-rotor turbines with different tip spacings. $\Delta U(x,y,z) = U(-1D,y,z) - U(x,y,z)$ and $\Delta U_{disk}(x) = \int_{disk} \Delta U(x,y,z)\mathrm{d}y\mathrm{d}z$, with the integral carried out over one circle in the $y-z$ plane of diameter D for the 1-rotor turbine and over four different circles in the $y-z$ planes with diameters d for the 4-rotor turbines.

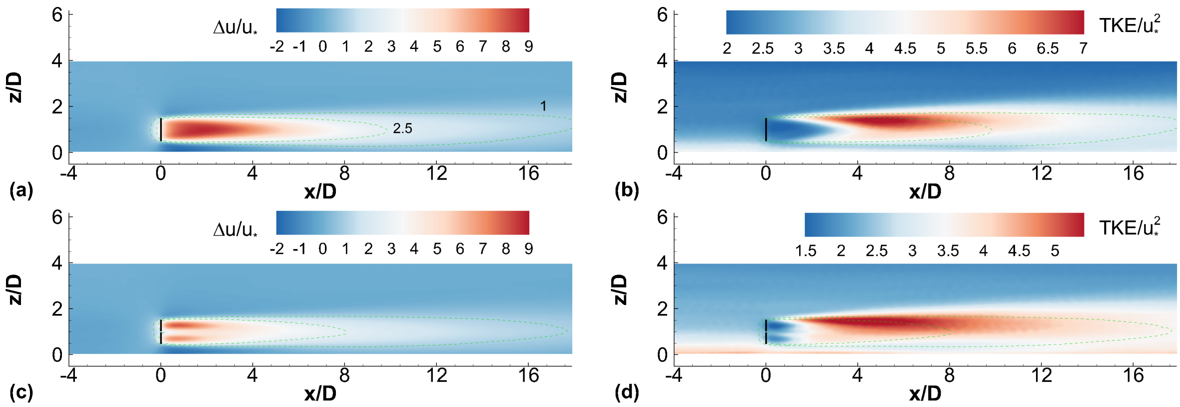

Figure 3. ABL-turbine interaction simulation results. Contours of (a,c) mean streamwise velocity deficit and (b,d) TKE at the centerline, for (a,b) 1-rotor turbine and (c,d) 4-rotor turbine with $s/d = 0.1$. Black solid lines denote turbine rotor disks. Dashed lines denote specific selected contours of velocity deficit.

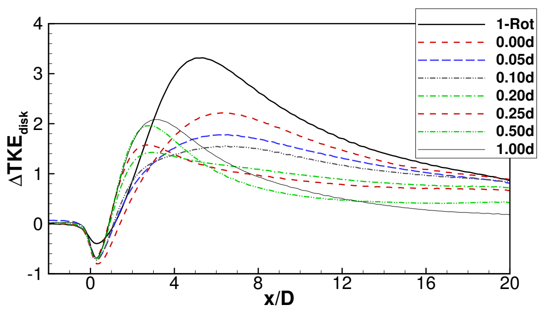

Figure 4. Disk-averaged added TKE as a function of axial distance for 1-rotor turbine and 4-rotor turbines with different tip spacings. $\Delta TKE(x,y,z) = TKE(x,y,z) - TKE(-1D,y,z)$ and the disk-average is carried out as described in caption to Figure 2.

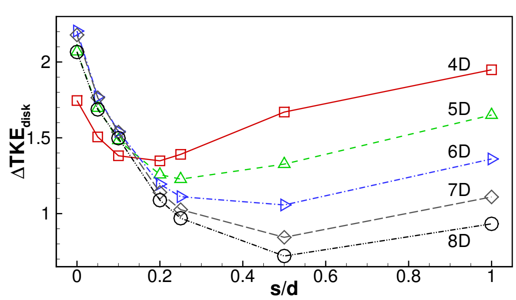

Figure 5. ABL-turbine interaction simulation results. Disk-averaged added TKE as a function of tip spacing at different downstream locations noted in the figure labels.

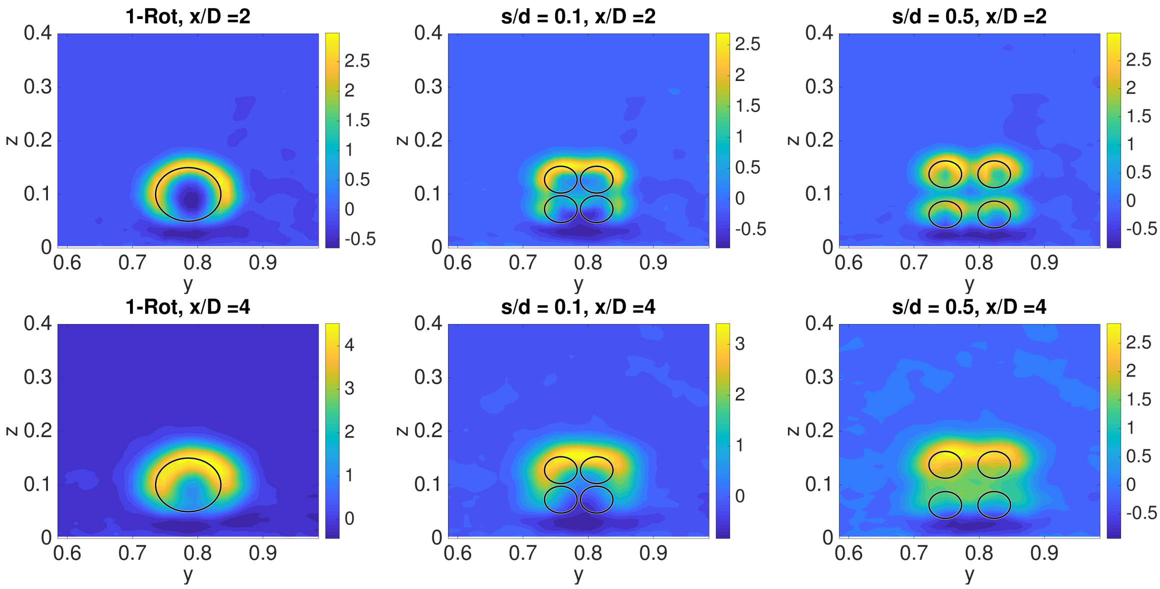

Figure 6. ABL-turbine interaction simulation results. Added TKE contours in $y-z$ plane at different axial locations and for different cases noted in the figures.

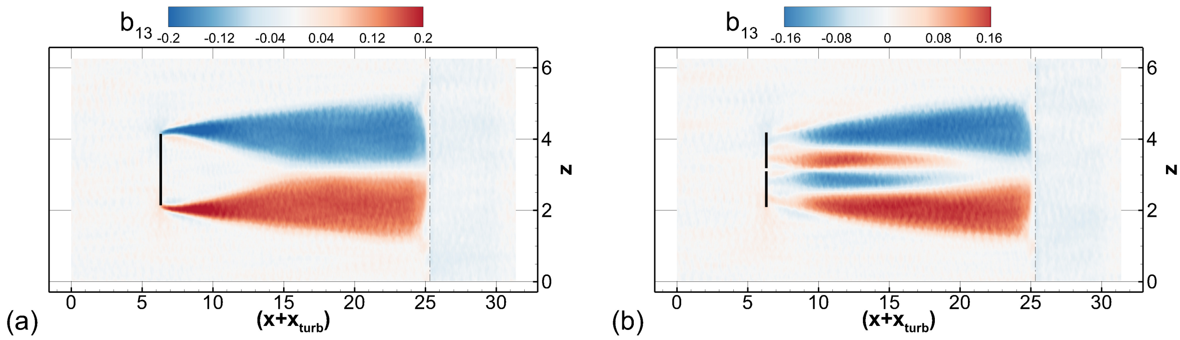

Figure 7. HIT-turbine interaction simulation results. Contours of 13− component of the anisotropy tensor, $b_{ij} = R_{ij}/R_{kk} - \delta_{ij}/3$, where R_{ij} is the Reynolds stress tensor for (a) 1-rotor case, and (b) 4-rotor case with tip spacing $s/d = 0.1$. Turbine ADs are denoted by solid lines, located at $x = 0$. Distance to the turbine from the start of the domain in the $x-$direction is $x_{turb} = 2\pi$. Diameter of 1-rotor turbine is $D = 2$ and individual rotors of the 4-rotor turbine have diameters $d = D/2 = 1$. Vertical dash-dotted line at approximately $x + x_{turb} = 25$ marks the beginning of the buffer region used for forcing the simulations.

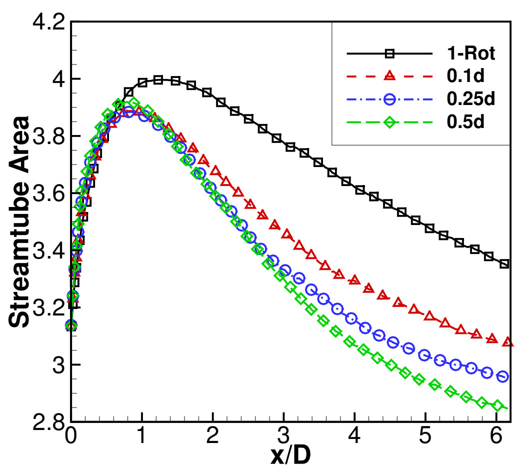

Figure 8. HIT-Turbine Interaction Simulations. Area of cross-section of streamtubes originating at the rotor disk(s). Subsequent analysis focuses on averages computed over these cross-sectional areas.

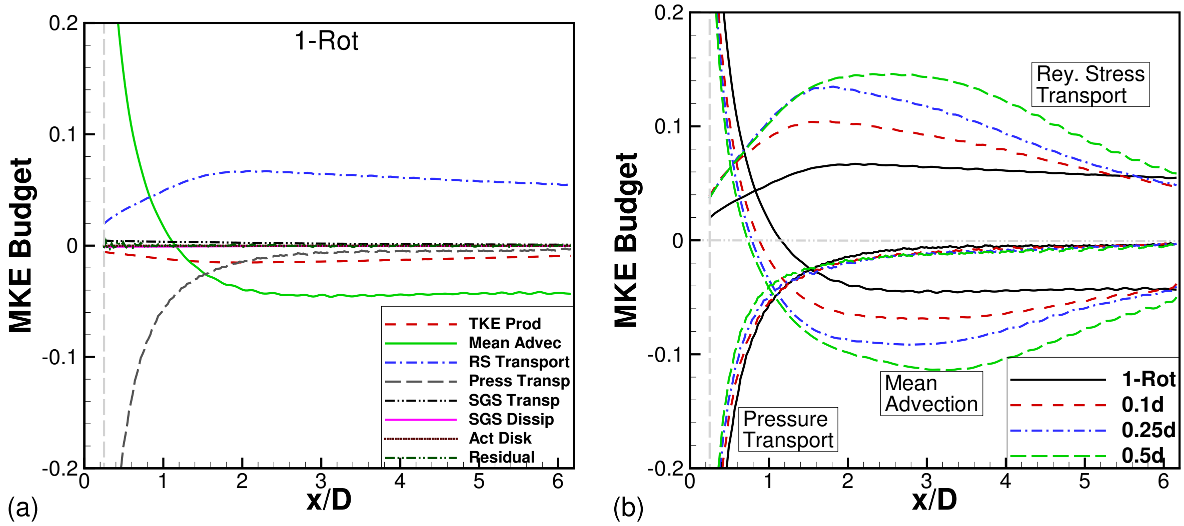

Figure 9. HIT-turbine interaction simulation results. Streamtube-averages of terms in the Mean Kinetic Energy (MKE) equation for (a) 1-rotor case, and (b) 4-rotor turbines with varying tip spacing, s, noted in the legend. Only three dominant terms are shown in (b). Turbine ADs are located at $x/D = 0$. Vertical dashed line marks end of very near-disk region. Horizontal dash-dot-dot line shows zero level.

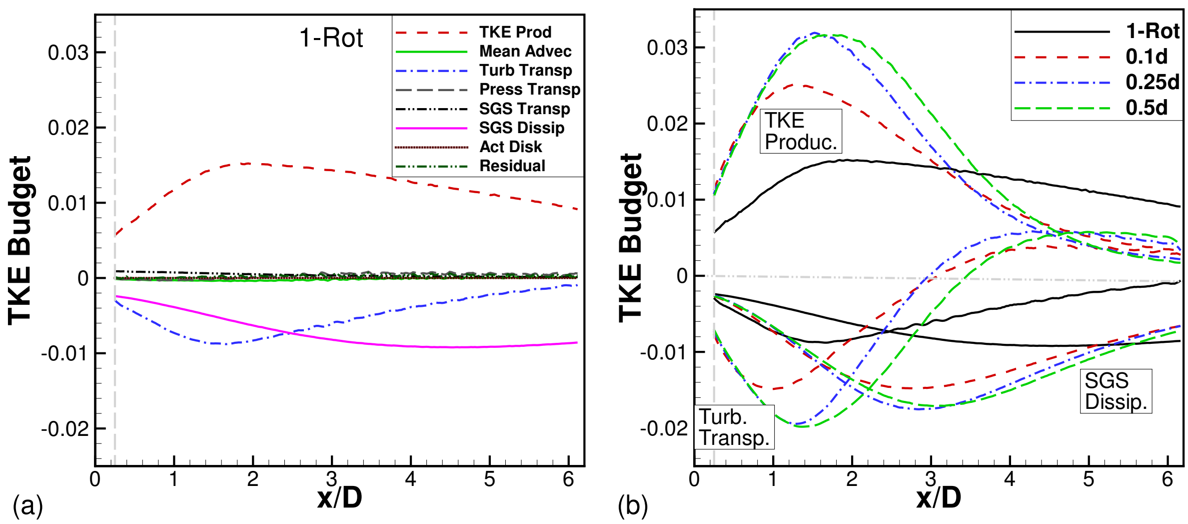

Figure 10. HIT-turbine interaction simulation results. Streamtube-averages of terms in the Turbulent Kinetic Energy (TKE) equation for (a) 1-rotor case, and (b) 4-rotor turbines with varying tip spacing, s, noted in the legend. Only three dominant terms are shown in (b). Turbine ADs are located at $x/D = 0$. Vertical dashed line marks end of very near-disk region. Horizontal dash-dot-dot line shows zero level.